Volume 13
Number 40
28 October 2025
Pages 12691–13112

# Journal of Materials Chemistry B

Materials for biology and medicine

rsc.li/materials-b

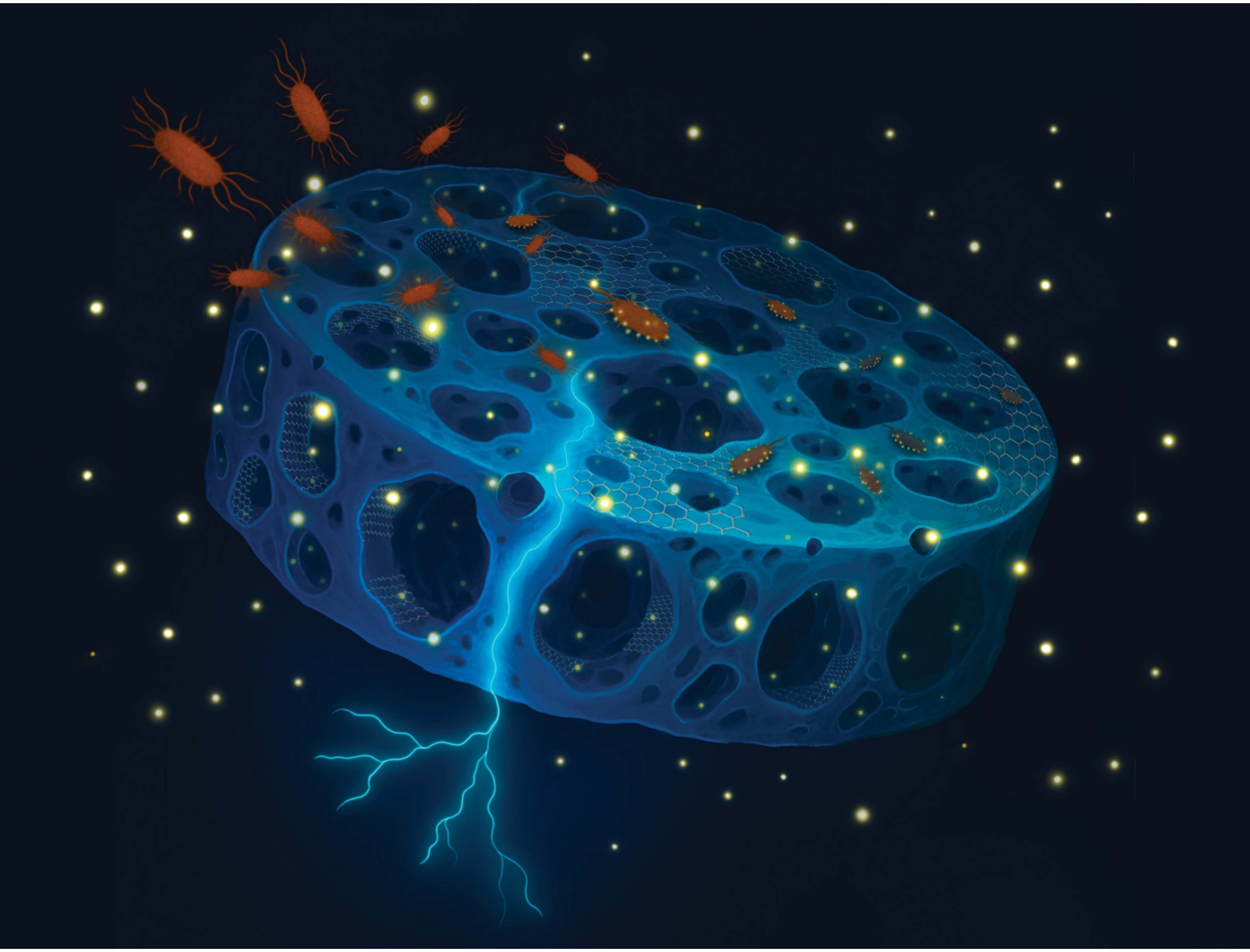

ISSN 2050-750X

ROYAL SOCIETY OF CHEMISTRY

**COMMUNICATION**
Charalampos Pitsalidis *et al.*
Conducting composite scaffolds for antibacterial drug release and *in situ* electrochemical monitoring of bacterial growth

Journal of
Materials Chemistry B

ROYAL SOCIETY
OF CHEMISTRY

COMMUNICATION

View Article Online
View Journal | View Issue

Open Access Article. Published on 26 September 2025. Downloaded on 6/16/2026 10:00:02 AM.
This article is licensed under a Creative Commons Attribution-NonCommercial 3.0 Unported Licence.

Check for updates

Cite this: *J. Mater. Chem. B*, 2025, **13**, 12877

Received 23rd April 2025,
Accepted 12th August 2025

DOI: 10.1039/d5tb00955c

rsc.li/materials-b

# Conducting composite scaffolds for antibacterial drug release and *in situ* electrochemical monitoring of bacterial growth

Khulood H. Alshehhi,[a] Deema Islayem,[b] Shahd B. Alshehhi,[bc] Bushara Fatma,[a]
Abdulrahim A. Sajini[bd] and Charalampos Pitsalidis *[aef]

**Conducting polymer scaffolds have gained significant attention as dynamic platforms for interfacing with biological systems, particularly in bioelectronic and tissue engineering applications. However, their potential in antimicrobial therapy and infection-responsive drug delivery remains unexplored. This study presents a multifunctional scaffold system based on PEDOT:PSS/MXene composites loaded with tetracycline hydrochloride (TCH), designed to deliver an antibacterial agent and monitor bacterial proliferation. By tuning the ratio of conducting polymer to MXene, we demonstrate composition-dependent control over drug release kinetics, with MXene-rich scaffolds exhibiting sustained release and enhanced antibacterial efficacy. Importantly, we also integrate electrochemical impedance spectroscopy as a label-free, real-time monitoring tool to track bacterial growth on the scaffold. Finally, we demonstrate the drug release from the scaffolds as triggered *via* electrostimulation. Overall, our approach establishes a dual-function platform that combines therapeutic drug delivery with real-time electrochemical monitoring, offering valuable insights into bacterial interactions with 3D scaffolds. These findings establish PEDOT:PSS/MXene composite scaffolds as an infection-responsive system, advancing their potential in next-generation wound healing and antimicrobial therapies.**

## 1. Introduction

Bacterial infections remain a significant challenge in healthcare and biomedical applications, particularly in wound care, where persistent infections can delay healing and lead to severe complications. The development of new bioactive and antimicrobial materials has become essential to address this issue, especially with the rise of antibiotic-resistant pathogens.[1,2] By tailoring material composition, microstructure, and device architecture, researchers can create multifunctional systems that actively inhibit bacterial colonization, promote therapeutic delivery, and enable real-time monitoring of infection-related signals.[3–5] Among various materials, conducting polymers (CPs)[6,7] and 2D materials[8–10] have separately emerged as exceptionally promising candidates for antimicrobial applications, offering tunable electrochemical properties, structural adaptability, and bioactivity.

CPs, in particular, stand out due to their unique set of properties, such as ionic conductivity, tailorability, and biocompatibility, making them ideal materials for use in bioelectronic and biomedical devices.[11–14] When formed into 3D architectures (*i.e.*, porous scaffolds, hydrogels), CPs provide a biomimetic environment that promotes cell adhesion and growth, critical aspects for tissue engineering and regenerative medicine.[15–18] Furthermore, their large-area-to-volume ratio allows for creating high-density tissue models and for supplying bioactive compounds.[19,20]

Poly(3,4-ethylenedioxythiophene) polystyrene sulfonate (PEDOT:PSS, P : P) has been widely applied in biomedical applications, owing to its high electrical conductivity, biocompatibility, and ability to form stable composites with synthetic and naturally derived materials, as well as with nanomaterials.[21–23] P : P can be easily processed in various forms and is commonly used as a flexible and conductive interface for tissue engineering and sensors.[24,25] One of the key advantages of P : P-based systems lies in their responsiveness to electrical stimuli and their ability to selectively detect specific biomolecules.[26] P : P hydrogels, in particular, have demonstrated the capacity to undergo microstructural changes in response to thermal or electrical cues, enabling controlled drug release for localized therapeutic applications.[27] Similarly, microfluidic-spun fibers incorporating P : P have demonstrated

---

[a] *Department of Physics, Khalifa University, Abu Dhabi, UAE. E-mail: charalampos.pitsalidis@ku.ac.ae*
[b] *Department of Biomedical Engineering, Khalifa University, Abu Dhabi, UAE*
[c] *Department of Biological Sciences, Khalifa University, Abu Dhabi, UAE*
[d] *Department of Biology, Chemistry, and Environmental Sciences, American University of Sharjah, Sharjah, UAE*
[e] *Advanced Research and Innovation Center, Khalifa University, Abu Dhabi, UAE*
[f] *Foundation of Research and Technology Hellas, IESL Heraklion, Heraklion, Greece*

Open Access Article. Published on 26 September 2025. Downloaded on 6/16/2026 10:00:02 AM. This article is licensed under a Creative Commons Attribution-NonCommercial 3.0 Unported Licence.

tunable drug release under electrical stimulation, improving the release efficiency of drugs.[28] Moreover, P : P bioelectrodes have been employed in multifunctional platforms that combine drug delivery with real-time biosensing, allowing for the release of chemotherapeutic agents while simultaneously monitoring cell viability *via* impedance measurements.[29]

In parallel, 2D materials, such as graphene and MXenes, have also shown many interesting properties when incorporated into composite systems, such as improved mechanical properties, electrical conductivity, and surface tunability. MXenes, in particular, have gained momentum over the past decade due to their high surface area, hydrophilicity, and tunable surface chemistry.[30,31] Their chemical structure, consisting of transition metal carbides or nitrides, enhances their electrochemical activity, mechanical strength, and bio- and immune compatibility, making them highly suitable for biomedical technologies.[32,33] In antibacterial applications, MXenes have been found to act both as direct antibacterial agents,[8] causing physical membrane damage and oxidative stress, and as carriers for therapeutic agents, improving treatment efficiency.[34]

MXenes' excellent processability allows them to form and integrate into various architectures, including 3D scaffolds that support cellular interactions. While this is possible, their mechanical rigidity compromises their direct utilization in soft and flexible systems. As such, MXenes are often used in composite systems where they can be combined with polymers, hydrogels, or elastomers that retain the MXene's conductivity and bioactivity while improving their mechanical adaptability.[4,23,35–37] In particular, in biosensing, the abundant functional groups in MXene, in conjunction with the electrochemical activity of CPs (*i.e.*, redox-active polymers), allow for surface modifications with biomolecules, enzymes, and antibodies, enabling sensitive detection of biological analytes. Although these composite systems exhibit unique properties for tissue engineering and bioelectronics, research into their interactions with living organisms remains incomplete, leaving a gap in our understanding of their biocompatibility and bioactivity.

Following this rationale, in this work, we present the development of a tetracycline hydrochloride (TCH)-loaded scaffold based on a P : P and MXene composite system designed to address bacterial infection through drug release and electrochemical monitoring. Through a systematic investigation of scaffold composition, we demonstrate how MXene content influences drug release kinetics and antibacterial efficacy. Importantly, we integrate EIS as a label-free, *in situ* method for tracking bacterial growth dynamics on the scaffold surface. Finally, exploiting the electrochemical properties of the scaffold, we demonstrate the use of electrically triggered drug release. This study not only highlights the potential of the P : P/MXene composite system in infection-responsive applications, but also provides new insights into their structure–function relationships, establishing a route for future development of bioactive platforms for wound healing and beyond.

## 2. Experiments

### 2.1. Materials and methods

Poly(3,4-ethylene dioxythiophene) polystyrene sulfonate (PEDOT:PSS or P : P) (Clevios PH 1000, Heraeus), dodecylbenzene sulfonic acid (DBSA, Sigma-Aldrich), glycidoxypropyl-trimethoxysilane (GOPS, Sigma-Aldrich), and MXene ($Ti_3C_2T_x$) were utilized for scaffold fabrication. Tetracycline hydrochloride (HiMedia) was incorporated into the scaffolds for drug release studies, with Dulbecco's phosphate-buffered saline (DPBS, Gibco) serving as the release medium. All reagents were used as received without further purification. The fabrication and characterization processes were performed using various analytical instruments. Scaffold structures were prepared using an SP Virtis Advantage Pro freeze dryer. Drug release and bacterial studies were conducted by analyzing the absorbance at 270 nm and 600 nm, respectively, using an Infinite M200 Pro UV-Vis plate reader. Weight measurements were recorded using a Kern ABS 220-4N analytical balance, while electrical characterization of the scaffolds was carried out with an Ossila four-point probe. Morphological analysis and bacterial adhesion studies were performed using scanning electron microscopy (SEM), employing a Quanta 250 FEG and a Phenom XL Desktop SEM. The latter was also used for elemental analysis to facilitate material identification. EIS measurements were performed using a Palmsens 4 potentiostat. ES was conducted using a dual-channel arbitrary function generator (GW Instek, MFG-2260MRA).

### 2.2. MXene preparation

$Ti_3C_2T_x$ MXene was synthesized from $Ti_3C_2Al$ MAX phase ($\leq$40 μm) using a minimally intensive layer delamination (MILD) method. Selective aluminium removal was achieved *via in situ*[38] lithium fluoride etching. A solution was prepared by dissolving 1.6 g of LiF in 20 mL of 9 M hydrochloric acid (HCl), followed by the gradual addition of 1 g of MAX phase powder. The mixture was stirred for 24 hours at room temperature to facilitate etching. The resulting dispersion was washed multiple times with deionized water and centrifuged at 3500 rpm for 6 minutes per cycle until the pH exceeded 6, yielding a dark green colloidal suspension of single- or few-layer $Ti_3C_2T_x$ flakes. The purified MXene was stored at −80 °C, while the unetched MAX residue was discarded. MXene concentration was determined *via* vacuum filtration, yielding 8.32 mg $mL^{-1}$. The suspension was subsequently diluted with autoclaved double-distilled water (18 MΩ) to obtain a 2 mg $mL^{-1}$ solution, with a final concentration of 1 mg $mL^{-1}$ used in this study.

### 2.3. Fabrication of drug-loaded scaffolds

P : P/MXene composite solutions were freeze-dried to achieve a porous structure. Specifically, a 10 mL solution of P : P was sonicated for 10 minutes, then 0.05 g of DBSA was added, with an additional 5-minute sonication. To enhance scaffold stability, 0.3 g of GOPS was incorporated, and the solution was sonicated for another 5 minutes before undergoing magnetic stirring for 30 minutes to ensure uniform dispersion.

Open Access Article. Published on 26 September 2025. Downloaded on 6/16/2026 10:00:02 AM. This article is licensed under a Creative Commons Attribution-NonCommercial 3.0 Unported Licence.

A 1% (w/v) MXene dispersion was mixed with P : P in varying ratios to produce scaffolds with different compositions. Each well of a 48-well plate was filled with 500 μL of the composite solution in P : P/MXene ratios of 3 : 1, 2 : 1, 1 : 1, 1 : 2, and 1 : 3, along with a control group consisting of P : P-only scaffolds (P : P). TCH was incorporated into the scaffolds by adding 50 μL of a 50 mg $\mathrm{mL}^{-1}$ TCH solution to each well, resulting in a final TCH concentration of 0.5% (w/v). The 48-well plate was then freeze-dried to produce porous scaffolds, which were subsequently baked at 80 °C for 5 hours. The dried scaffolds were sliced for further analysis.

### 2.4. Electrical and electrochemical characterization

The electrical properties of the scaffolds were measured using a four-point probe conductivity method. The resistivity ($\rho$) of the scaffolds was calculated using the equation:

$$\rho = 2\pi S\frac{V}{I}\left[\Omega\,\mathrm{cm}^{-1}\right] \tag{1}$$

where $S$ is the probe spacing, $V$ is the measured voltage, and $I$ is the applied current. For these measurements, cylindrical scaffold samples were prepared (8 mm diameter, 600 μm thickness), and measurements were repeated on three different scaffolds for each composition to ensure reproducibility. EIS was also performed to analyze the impedance behavior of the scaffolds. These measurements provided insights into their electrochemical properties, both with and without TCH loading, facilitating a deeper understanding of the scaffolds' conductive and capacitive characteristics.

### 2.5. Cumulative drug release

The cumulative drug release was evaluated by monitoring TCH diffusion into PBS at 37 °C under gentle agitation. Each scaffold was incubated in 2 mL buffer, with 100 μL samples withdrawn at specific time points and replaced with fresh buffer. All measurements were performed in triplicate for reproducibility.

The concentration of TCH in each sample was determined using UV-Vis spectroscopy (270 nm), based on the linear calibration equation:

$$C_{\mathrm{TCH}}\ (\mu\mathrm{g\ mL}^{-1}) = (\mathrm{slope} \times \mathrm{absorbance}) \pm \mathrm{intercept} \tag{2}$$

To account for the sampled volume replacement, the cumulative drug release (%) was calculated using:

$$\text{Cumulative release}\ (\%) = \frac{V_{\mathrm{s}}\ (\mathrm{mL})}{V_{\mathrm{b}}\ (\mathrm{V})} \times P_{t-1} + P_t \tag{3}$$

where $V_{\mathrm{s}}$ is the sample volume (0.1 mL), $V_{\mathrm{b}}$ is the total bath volume 2 mL, $P_{\mathrm{t}}$ is the percentage released at the current time, and $P_{\mathrm{t-1}}$ is the previous cumulative release percentage.

### 2.6. Swelling studies

The swelling behavior of the P : P/MXene scaffolds was assessed by measuring weight changes at specified time points following immersion in water. All experiments were conducted in triplicate, and results are reported as the mean ± standard error (SE) from three samples, each maintained in separate containers. Initially, the dry weight of each scaffold ($W_{\mathrm{d}}$) was recorded. The scaffolds were then placed in well plates, fully immersed in water, sealed, and stored at room temperature for the duration of the test. Liquid uptake, or swelling, was assessed by weighing the scaffolds at 24-hour intervals. Each sample was carefully removed, gently blotted with filter paper to remove excess surface water, and weighed to determine the wet weight ($W_{\mathrm{w}}$). The swelling ratio was calculated using the following formula:

$$\text{Swelling ratio}\ (\%) = \frac{W_{\mathrm{w}} - W_{\mathrm{d}}}{W_{\mathrm{d}}} \times 100 \tag{4}$$

A graph was generated to show the change in the swelling index over time based on the average values obtained. This procedure allowed for the quantitative evaluation of scaffold liquid uptake and structural stability under aqueous conditions.

### 2.7. Bacterial growth conditions

*E. coli* (ATCC 25922), *P. aeruginosa* (ATCC 15692), and *S. aureus* (ATCC 12600) were revived from a glycerol stock by streaking onto an LB agar plate and incubating at 37 °C for 24 h. Single colonies were then picked up and inoculated into LB broth and incubated in a shaker incubator at 120 rpm and 37 °C for 24 h. After incubation, the optical density (OD) of the bacterial culture representing its growth was measured at a wavelength of 600 nm ($\mathrm{OD}_{600}$) using a plate reader. The culture was subsequently diluted with fresh LB broth to an $\mathrm{OD}_{600}$ of 0.2, representing the exponential growth phase, making it ready for further experiments. It should be noted that TCH primarily exhibits absorbance peaks at wavelengths below 400 nm, with negligible absorbance at 600 nm; therefore, it does not interfere with $\mathrm{OD}_{600}$ measurements. Thus, the recorded values reliably reflect bacterial density, independent of the presence of the TCH.[39]

### 2.8. Antibacterial studies

The antibacterial efficacy of the scaffolds was evaluated using three complementary approaches to comprehensively assess their activity against bacterial strains. In the first method, identical scaffold slices were incubated in 2 mL of buffer at 37 °C, and 100 μL samples were collected at predetermined time intervals. These buffer samples, containing the TCH released from the scaffolds, were mixed with bacterial suspensions of *P. aeruginosa* and *E. coli* and incubated further for 4 h and 16 h, with bacterial growth monitored by measuring $\mathrm{OD}_{600}$. This method was used to assess the indirect antibacterial effect of drug release. In the second approach, the scaffold slices were directly immersed in bacterial media containing *E. coli*, *P. aeruginosa*, and *S. aureus*, and incubated at 37 °C for 24 hours. After incubation, scaffolds were fixed in 2% glutaraldehyde, dehydrated using graded ethanol solutions, and examined *via* SEM to evaluate bacterial adhesion and morphology, alongside corresponding $\mathrm{OD}_{600}$ measurements of the media to assess bacterial growth. In the third approach to quantitatively assess antibacterial activity, a colony forming

Open Access Article. Published on 26 September 2025. Downloaded on 6/16/2026 10:00:02 AM.
This article is licensed under a Creative Commons Attribution-NonCommercial 3.0 Unported Licence.

unit (CFU) assay was performed after 24 hours of incubation. A bacterial suspension was collected from each scaffold composition and serially diluted in PBS. For *P. aeruginosa* and *E. coli*, six 1:10 serial dilutions were performed (final dilution $10^{-6}$), while for *S. aureus*, four 1:10 dilutions were used (final dilution $10^{-4}$). Then, 40 μL was spread on LB agar plate and incubated at 37 °C for 24 hours. Colonies were then counted, and CFU $\mathrm{mL}^{-1}$ was calculated using the following formula:

$$\mathrm{CFU\ mL^{-1}} = (\text{number of colonies} \times \text{dilution factor})/\text{volume plated (in mL)} \quad (5)$$

### 2.9. Electrochemical impedance spectroscopy measurements

EIS was employed to monitor bacterial growth and scaffold–electrolyte interfacial changes in real time. A custom-made three-electrode platform was developed to enable consistent scaffold positioning and measurement reproducibility. Patterned gold electrodes were cut to serve as the working electrode (WE), making lateral contact with the conductive scaffolds. Each scaffold was held in place using a 3D-printed holder slotted into a standard 6-well plate, interfaced with a transparent insert to ensure immersion and electrical connection. A stainless-steel mesh was used as the counter electrode (CE), and an Ag/AgCl electrode as the reference electrode (RE). Two interchangeable lids were used: a sterile lid for incubation and a measurement lid with ports for electrode insertion. All components were sterilized between uses. Impedance spectra were recorded using a potentiostat over a frequency range of 0.1 Hz to 100 kHz, applying a 10 mV AC perturbation at open circuit potential. Measurements were performed at five time points (0 h, 2 h, 4 h, 8 h, and 16 h) during incubation at 37 °C. Three scaffold compositions were tested: pristine P:P, P:P/MXene (1:1), and P:P/MXene (1:3). For each composition, three experimental conditions were evaluated: (i) scaffolds in LB broth without bacteria but with TCH, (ii) scaffolds in *E. coli*-inoculated LB broth without TCH, and (iii) scaffolds in *E. coli*-inoculated LB broth containing TCH. *E. coli* cultures were diluted in fresh LB medium to a final $\mathrm{OD}_{600}$ of 0.2, and 5 ml was added to each well. This matrix design enabled systematic evaluation of the effects of scaffold composition, drug loading, and bacterial colonization on the impedance response. Changes in impedance over time provided quantitative data on bacterial interaction with the scaffold surface, complementing $\mathrm{OD}_{600}$ measurements and SEM imaging.

### 2.10. Electrical stimulation experiments

Electrically triggered drug release experiments were conducted using various TCH-loaded scaffolds. The experimental setup involved a custom-designed well plate platform. In each well plate, two wells were connected to a DC-stimulator (waveform generator), while the third served as an unstimulated control. The system employed a two-electrode configuration, with the scaffold (interfaced with a gold electrode) serving as working electrode and a stainless-steel mesh as the counter electrode, both fully immersed in PBS (or medium). Three stimulation conditions were tested: (i) positive stimulation (+0.8 V, scaffold as anode), (ii) negative stimulation (−0.8 V, scaffold as cathode), and (iii) neutral control (no stimulation). The square pulse frequency of the signal was 0.5 Hz. Scaffold formulations tested involved pristine P:P, and P:P/MXene composites at 1:1 and 1:3. For each condition, triplicate samples ($N = 3$) were prepared. At predefined time-points (5, 15, 30 min; 1, 2, 4, 8, and 16 h), 200 μL of the supernatant was collected from each well. TCH release was measured using UV–Vis spectroscopy at 270 nm, and cumulative release was calculated as a percentage of the total drug content loaded in each scaffold.

## 3. Results and discussion

### 3.1. Scaffold characterization

Fig. 1a illustrates the chemical structures of the scaffold components and the key molecular interactions between P:P, MXene, and TCH. We hypothesize that these involve hydrogen bonding that can be formed between hydroxyl, amine, and carbonyl groups of TCH and the –OH and –F groups of MXene, as well as with the $-\mathrm{SO_3}^-$ groups of P:P. In addition, electrostatic interactions can arise between the negatively charged sulfonate groups of PSS and the positively charged amine groups of TCH. Other intermolecular interactions may also be involved, such as coordination bonds and π–π interactions.

Fig. 1b illustrates the step-by-step processing of the scaffolds, beginning with the preparation of the P:P solution and its mixing with MXene at different volume ratios (ranging from 3:1 to 1:3). Subsequently, TCH is introduced into the composite mixture, ensuring uniform dispersion. Upon proper intermixing, the resulting solution undergoes a freeze-drying process, removing the water content through ice-sublimation, resulting in a porous scaffold architecture like previously reported P:P-based scaffolds.[15,19,40–42] A detailed schematic of the fabrication process is also shown in Fig. S1. To ensure reproducibility, the resulting scaffolds are sliced into identical, uniform, thin sections. This format allows for improved handling and enables more precise control over the bacterial/cell seeding process by promoting uniform distribution and penetration across the scaffold surface[15,43] (see Fig. S2).

The photographic images in Fig. 1c illustrate the visual changes in color of the various scaffolds, clearly transitioning from bright green to black as the MXene content increases. The corresponding SEM images reveal the morphological characteristics of the composite scaffolds, displaying a 3D network of interconnected macroscale pores distributed throughout the sample. The images highlight variations in pore size and morphology across the different ratio conditions, demonstrating a trend of increased pore size with higher MXene, content from 157.5 ± 42.2 μm in 1:3 to 266.1 ± 54.8 μm (see also Fig. S3, S4 and Table S1). This can be attributed to the increased water content upon the addition of MXene solution to the P:P mixture, which in turn leads to the formation of larger ice crystals during the freeze-drying process. As a result, the sublimation of these larger ice crystals leads to an enlarged

Open Access Article. Published on 26 September 2025. Downloaded on 6/16/2026 10:00:02 AM.
This article is licensed under a Creative Commons Attribution-NonCommercial 3.0 Unported Licence.

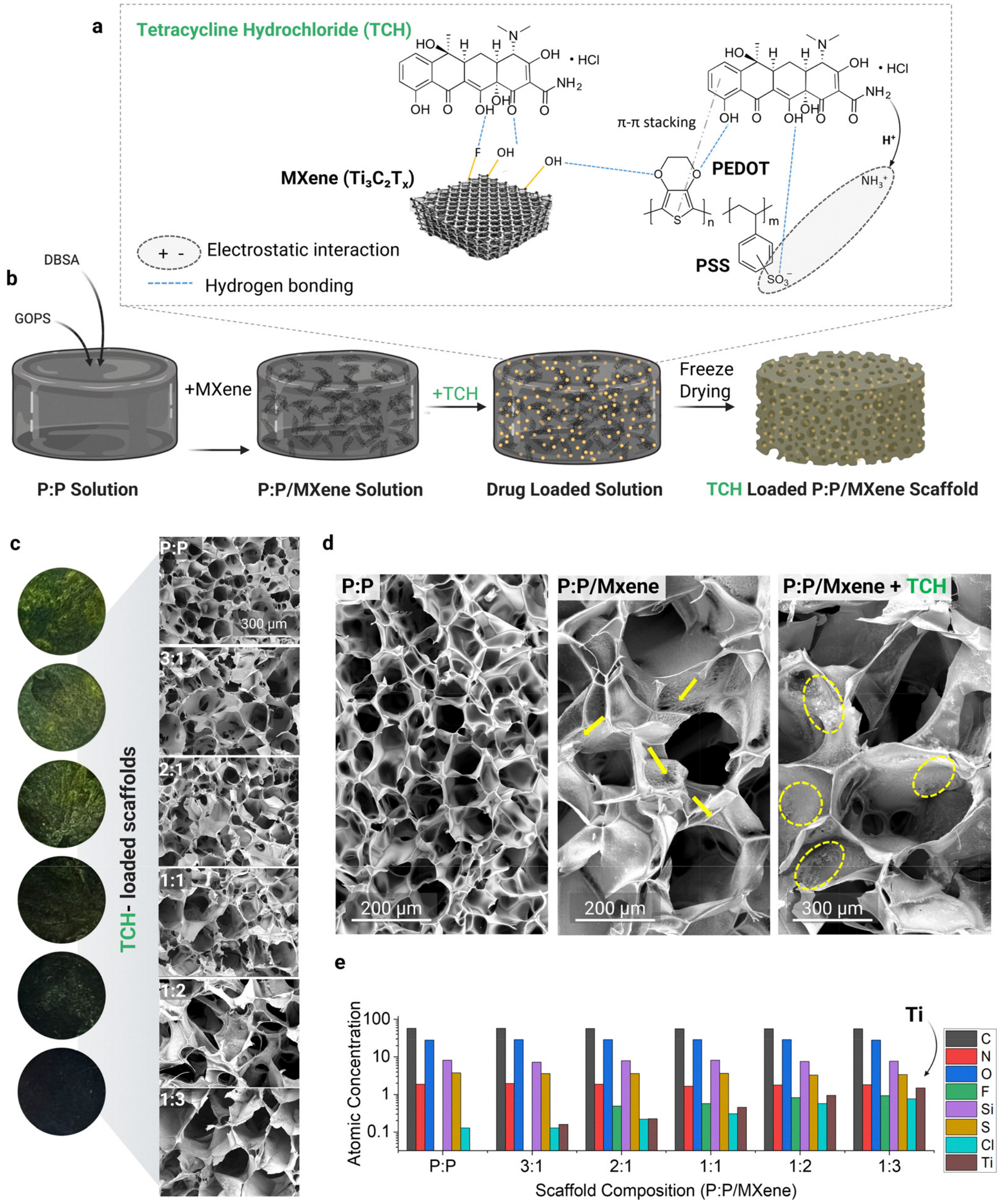

Fig. 1 (a) Chemical composition of the composite scaffolds and schematic representation of the molecular interactions within the P : P, MXene, and TCH. (b) Process steps for the preparation of the composite scaffolds. (c) Photographic and corresponding SEM images showing the porous structure of the freeze-dried scaffolds. (d) Magnified SEM images showing a detailed view of the pore surface for P : P, P : P/MXene, and TCH-loaded P : P/MXene (1 : 3). Yellow arrows indicate nanotextured formations on the pore surface associated with the presence of MXene. The dashed circles in the TCH-loaded P : P/MXene scaffolds highlight regions with granular formations onto the pores. (e) EDX analysis of the composite scaffolds showing the elemental composition. The arrow indicates the increase in the titanium content with increasing MXene content.

pore structure within the scaffold. As shown in Fig. 1d, the introduction of MXene in the P : P phase introduces nanotextured domains, which become more pronounced as the MXene content increases (see Fig. S5). At the same time, the scaffold morphology exhibits noticeable changes upon the incorporation of TCH, with distinct granular formations onto the pores' surface, as highlighted in the same figure (see also Fig. S6). These morphological modifications suggest a tunable scaffold architecture that may determine several properties and functionalities, including drug-loading capability, bioactivity, and electrochemical performance.

The elemental composition of the scaffolds is analyzed using EDX, as shown in the histogram of Fig. 1e. Titanium (Ti), a signature element in MXene, is detected in all composite scaffolds, with its presence increasing proportionally to the MXene content. Furthermore, the presence of chlorine (Cl), which corresponds mainly to the TCH, further validates the incorporation of the drug within the scaffolds. Interestingly,

Open Access Article. Published on 26 September 2025. Downloaded on 6/16/2026 10:00:02 AM.
This article is licensed under a Creative Commons Attribution-NonCommercial 3.0 Unported Licence.

the Cl signal appears to intensify with increasing MXene content, even though the same amount of TCH is used in all conditions. This indirectly confirms TCH's tendency to bind to MXene through electrostatic interactions and hydrogen bonding, owing to the abundant functional groups present in both components. Such intermolecular interactions may enhance TCH retention on and within the scaffold and can play a critical role in modulating the release kinetics.

### 3.2. Conductivity and electrochemical properties of scaffolds

The electrical properties of the scaffolds are evaluated using four-probe measurements to understand the influence of MXene and TCH loading on the conductivity of the scaffolds. Fig. 2a presents a comparative histogram with the sheet resistance values of the various P:P/MXene scaffolds, with and without TCH. The measured data reveal a significant increase in sheet resistance, from 0.32 (±0.06) kΩ $sq^{-1}$ in 3:1 to 10.8 (±0.18) kΩ $sq^{-1}$ in 1:3, upon TCH loading. This rather odd effect is likely due to the disruption of the conductive polymer network caused by TCH, which compromises charge transport efficiency. Specifically, the pronounced binding of TCH at higher MXene ratios may introduce more insulating domains within the bulk of the scaffold, further decreasing their electrical conductivity (see Fig. S7). Notably, even without the incorporation of TCH, the scaffolds exhibit a progressive decline in their conductivity with increasing MXene content. While the MXene alone can provide highly conducting nanodomains, the charge transfer properties are predominantly dependent on the P:P network. We hypothesize that mixing the P:P solution with the MXene solution at high ratios (*i.e.*, 1:2 or 1:3) leads to dilution of the conducting P:P phase, thereby affecting the electronic properties of the resulting composite. Furthermore, raising the water content in the mixture impacts both the pore size and scaffold architecture, which can subsequently affect the charge percolation pathways.

A custom-built three-electrode electrochemical cell is used to investigate further the impact of MXene and drug loading on the electrochemical properties of the scaffolds. As shown in the EIS Bode plot of Fig. 2b, the scaffolds with higher MXene content steadily increase the overall complex impedance magnitude ($|Z|$). Specifically, at high frequencies, the observed increase in ($|Z|$) reflects alterations in the ohmic (resistive) regime at the electrode/electrolyte interface, which can be attributed to structural rearrangements introduced by the TCH and MXene, as explained above. At mid-to-low frequencies, the lower P:P ratios show a major increase in the impedance magnitude, associated with changes in their capacitance. In addition, ion diffusion limitation may contribute to this effect as MXene (and TCH) may introduce barriers hindering ion transport. The Bode phase plot Fig. 2c, further supports these observations, showing a peak shift to lower frequencies with increasing MXene content. Additionally, the increase in phase values with the MXene ratio suggests a transition toward a capacitive behavior, possibly due to surface polarization effects caused by changes in the surface area of the porous electrodes.

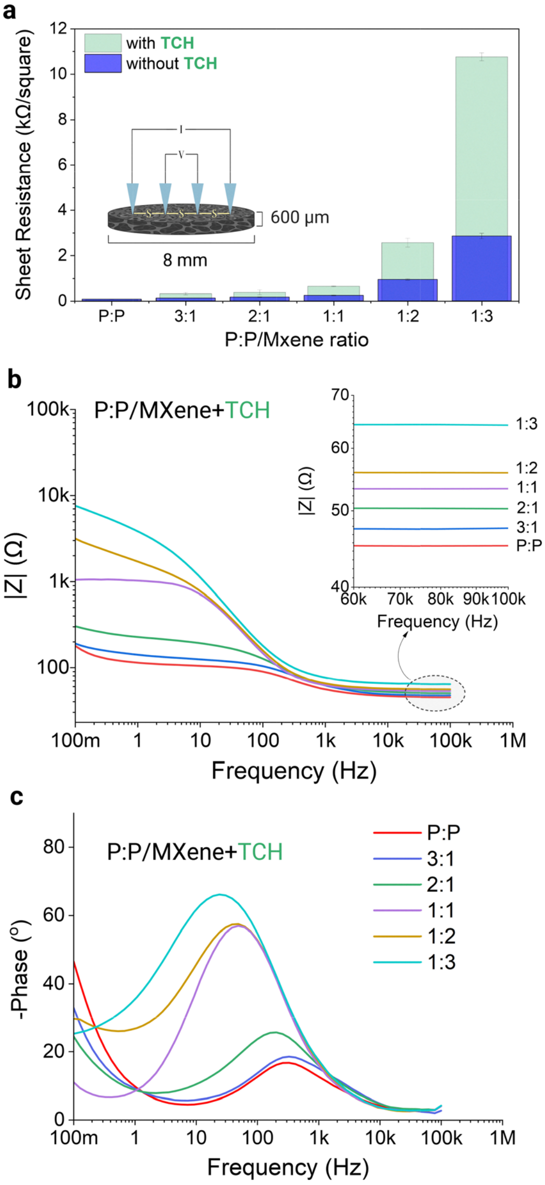

Fig. 2 (a) Sheet resistance of scaffolds with varying P:P to MXene ratios, measured for three different scaffold slices per condition, with and without TCH. The inset shows the four-point measurement mode and the dimensional characteristics of the tested scaffolds. (b) EIS Bode magnitude and (c) phase spectra of the TCH-loaded scaffolds measured in PBS using a three-electrode electrochemical cell.

### 3.3. Drug release kinetics and antibacterial activity

To evaluate the release profile of TCH from the composite scaffolds, absorbance measurements have been performed to determine the cumulative percentage drug (CPD) release over time. As illustrated in Fig. 3a, the scaffolds are initially sectioned into uniform, identical slices, which are then immersed in PBS solution, allowing for the release of TCH. The absorbance of the solution was measured in the 260–360 nm range, with two prominent peaks recorded at ∼270 nm and ∼350 nm, corresponding to a strong characteristic $\pi \rightarrow \pi^*$ transition within the aromatic structures of TCH. The results reveal the

Open Access Article. Published on 26 September 2025. Downloaded on 6/16/2026 10:00:02 AM.
This article is licensed under a Creative Commons Attribution-NonCommercial 3.0 Unported Licence.

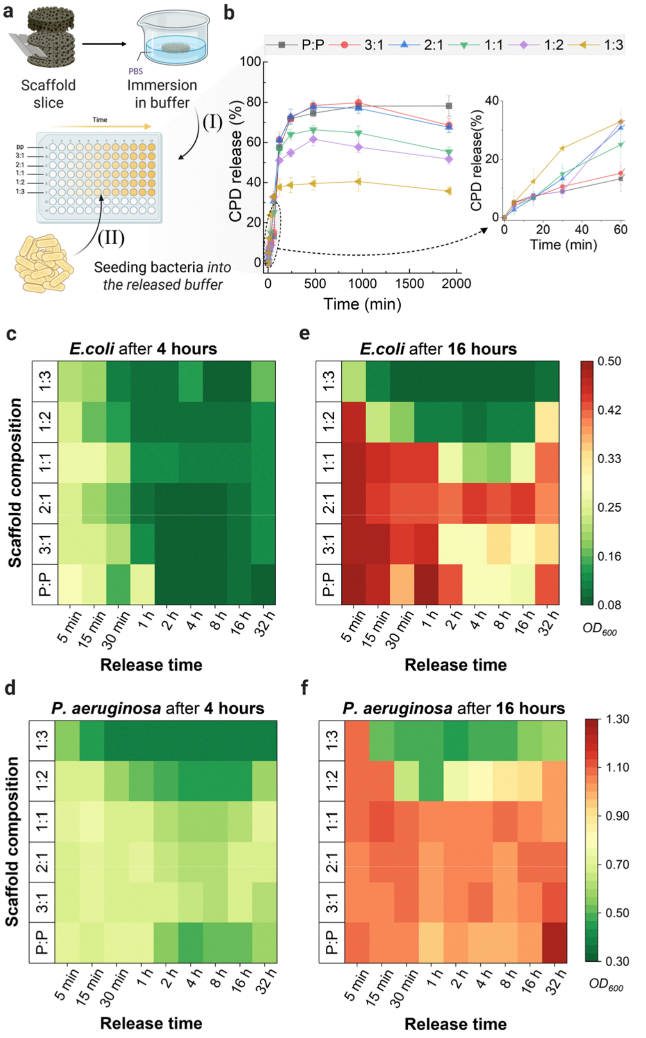

Fig. 3 (a) Schematic shows the experimental route for the evaluation of the TCH release effect on bacterial growth: (I) TCH release from the TCH-loaded scaffolds in a buffer solution (PBS), (II) seeding bacteria into the released buffer and measure the bacterial growth over time. (b) Graph shows the cumulative TCH release profiles for the various scaffolds over time ($N$ = 3). Heatmap plots showing antibacterial efficacy of the TCH-released solutions, determined by the extent of bacterial growth measured *via* $OD_{600}$, at different time intervals (from 5 min to 32 h) against *E. coli* and *P. aeruginosa* exposed for (c and d) 4 h and (e and f) 16 h, respectively.

release profile of TCH over time for each scaffold composition, demonstrating a biphasic release pattern (see Fig. 3b). Specifically, during the first 4 h, a burst release is observed for all the scaffolds, followed by a transition reaching a plateau at approximately 8 h. This initial burst release can be attributed to the rapid diffusion of TCH molecules that are adsorbed or loosely bound on the surface of the scaffolds. These molecules are readily accessible and dissolve quickly upon exposure to the release medium, resulting in a sharp increase in drug release. Notably, the initial release is more pronounced in the composite scaffolds and is found to increase with higher MXene content within the first hour (see inset of Fig. 3b), indicating a strong influence of MXene loading on the release kinetics. The high surface area, hydrophilicity, and layered nanostructure of MXenes can facilitate the adsorption of TCH molecules on the surface, which can be quickly released upon hydration. Furthermore, the plateau observed after the burst release phase indicates that the readily available TCH has been depleted, and the ongoing release process now mainly relies on TCH molecules embedded and/or strongly bound in the bulk of the scaffold. In such a case, the porosity and the swelling behavior of the scaffolds dictate their hydration and medium penetration, determining the overall TCH release. Specifically, an inverse trend emerges, with the higher MXene content scaffolds exhibiting a reduced CPD release. For example, while the 1 : 3 ratio is found to exhibit a higher release during the first hour, its maximum TCH release reached only 40.5 ± 4.8% after 16 hours. On the contrary, the pristine (P : P) scaffolds show a higher release value of 78.1 ± 3.6% after the same time. This observation is consistent with the swelling measurements of Fig. S8, which show a clear decrease in scaffold swelling capability with increasing MXene, supporting the correlation between reduced swelling and limited drug diffusion at later timepoints.

The antibacterial efficacy of the TCH-loaded scaffolds is assessed by introducing the corresponding released TCH solutions into bacterial cultures of *E. coli* and *P. aeruginosa*. Fig. 3c and d show the heatmap plots with the antibacterial efficacy of the TCH-released solutions against *E. coli* and *P. aeruginosa* after 4 h of exposure. The heatmaps reflect the extent of bacterial growth inhibition, as determined by $OD_{600}$ measurements, across various release time intervals (5 min to 32 h). For *E. coli*, during the initial phase (5 min to 1 h), all scaffolds show relatively similar antibacterial effects; however, scaffolds with higher MXene content demonstrated slightly better inhibition of bacterial growth compared to the other compositions. This suggests a more immediate antibacterial effect in scaffolds with higher MXene content, likely due to their pronounced TCH burst release, as shown previously. By the 2-hour mark and afterwards, all scaffolds, including the pristine ones (P : P), exhibited similar antibacterial activity, with reduced bacterial growth across all ratios. The P : P scaffold, in fact, demonstrated comparable inhibition with the MXene-rich scaffolds during this time, consistent with their TCH release profile. For *P. aeruginosa*, the effects of TCH release are more distinct, with higher MXene content scaffolds demonstrating enhanced antibacterial activity. The trends differ slightly from those observed with *E. coli*, as the 1 : 3 scaffold exhibits more pronounced antibacterial activity from the onset. Fig. 3e and f show the antibacterial effect of the TCH-released solutions after 16 h of exposure for both bacterial strains. In the case of *E. coli*, scaffolds with higher MXene content, particularly the 1 : 3, 1 : 2, and 1 : 1 composition, exhibited lower levels of bacterial growth beyond the 2-hour timepoint, suggesting more efficient antibacterial activity. In contrast, scaffolds with lower MXene content and the P : P displayed diminished efficacy over time, likely due to the depletion of TCH. A similar trend is observed for *P. aeruginosa*, with 1 : 3 scaffold demonstrating the most effective antibacterial activity, followed by the 1 : 2 composition.

Open Access Article. Published on 26 September 2025. Downloaded on 6/16/2026 10:00:02 AM.
This article is licensed under a Creative Commons Attribution-NonCommercial 3.0 Unported Licence.

These findings underscore the enhanced performance of the 1 : 3 scaffold in delivering immediate antibacterial activity against the two Gram-negative bacterial strains.

### 3.4. Direct antibacterial activity of the scaffolds

The inherent antibacterial activity of the scaffolds is further evaluated against both Gram-negative bacteria (*E. coli* and *P. aeruginosa*) and Gram-positive bacteria (*S. aureus*). Specifically, TCH-loaded scaffolds are placed in bacterial media containing the various bacterial strains and then incubated for 24 hours at 37 °C in LB broth (see Fig. 4a). The antibacterial activity is initially quantified by measuring the corresponding $OD_{600}$ of the immersed scaffolds (Fig. 4b), along with the CFU $mL^{-1}$ values (see Fig. S9). Subsequently, SEM imaging is performed on the same scaffolds, as shown in Fig. 4c–e. The $OD_{600}$ measurements and CFU $mL^{-1}$ reveal that bacterial growth decreases with increasing MXene concentration. Specifically, the P : P scaffold is found to give the highest $OD_{600}$ values, indicating the least inherent antibacterial efficacy. In contrast, the 1 : 3 scaffold composition demonstrates the lowest $OD_{600}$ and CFU $mL^{-1}$ values, confirming its superior antibacterial activity. The corresponding SEM imaging of the scaffolds further confirms these findings. As shown in Fig. 4c, the P : P scaffold shows extensive bacterial colonization of *E. coli*, with numerous bacteria adhering to the porous surface of the scaffold. With MXene concentration increasing, bacterial adhesion is found to decrease, and cell morphology deteriorates, indicating membrane disruption and bacterial lysis. Similar

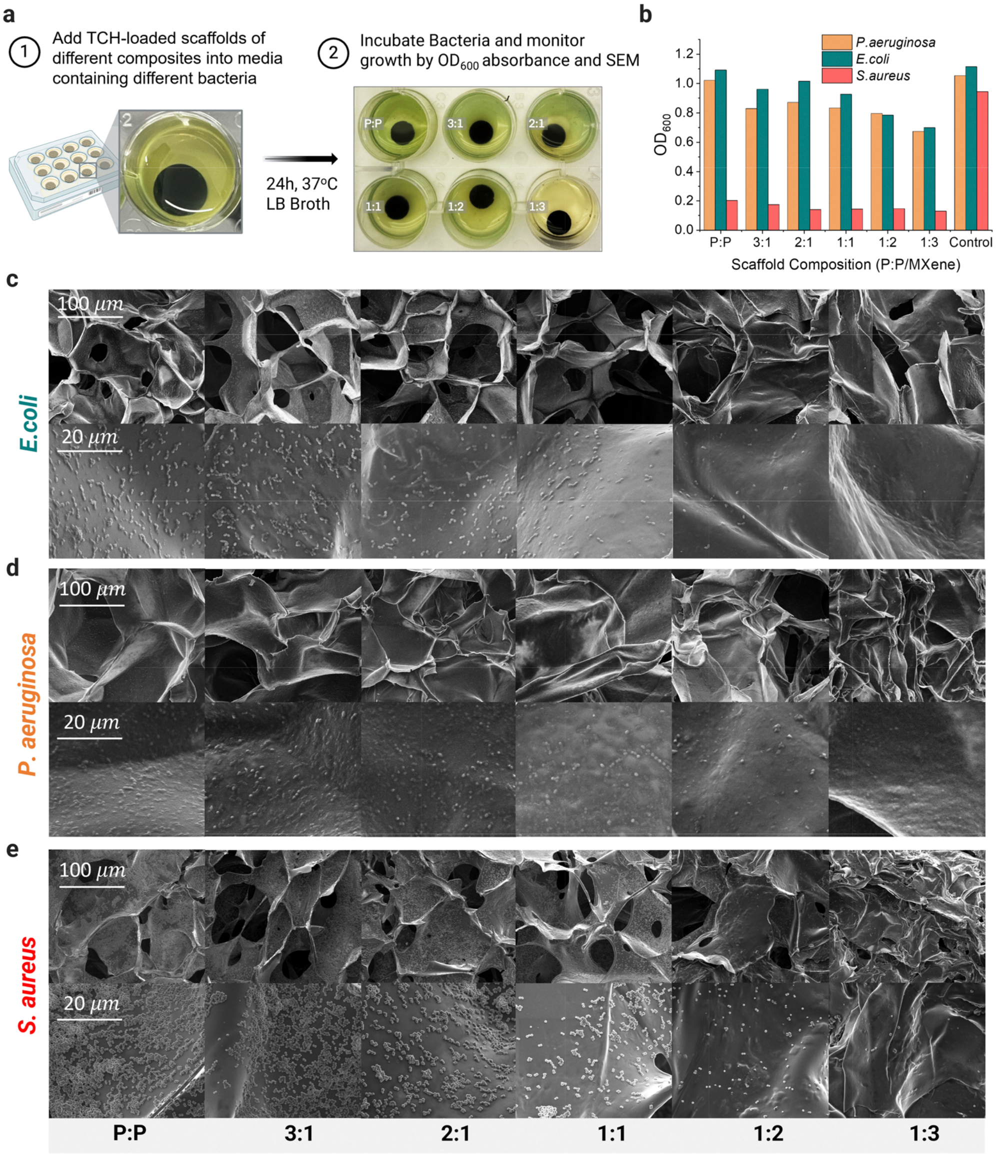

Fig. 4 Direct antibacterial activity of P : P/MXene scaffolds. (a) Schematic illustration of the experimental process for the study of the direct antibacterial activity of the scaffolds against various bacterial strains (*E. coli*, *P. aeruginosa*, and *S. aureus)* in bacterial media. (b) Bar graph showing the corresponding $OD_{600}$ values after 24 hours, indicating bacterial growth in media containing the scaffolds with varying P : P to MXene ratios. SEM images of (c) *E. coli*, (d) *P. aeruginosa*, and (e) *S. aureus* colonies on the various scaffolds after 24 h of incubation.

Open Access Article. Published on 26 September 2025. Downloaded on 6/16/2026 10:00:02 AM.
This article is licensed under a Creative Commons Attribution-NonCommercial 3.0 Unported Licence.

findings are found in the case of *P. aeruginosa* and *S. aureus*, as shown in Fig. 4d and e. Notably, while *S. aureus* displays relatively low $OD_{600}$ values, the corresponding SEM images reveal a pronounced surface adhesion, particularly on P:P-rich scaffolds. This outcome is consistent with literature reports that *S. aureus* has a strong tendency to adhere to surfaces and rapidly form biofilms, rather than remaining in planktonic form.[44,45] As a result, fewer bacteria remain in the surrounding medium, leading to relatively lower $OD_{600}$ values despite significant bacterial colonization on the scaffold.

While the released or surface-adhered TCH is expected to play a significant role in the antibacterial activity of the scaffolds, the intrinsic antimicrobial properties of MXene may also contribute to the observed effects. To investigate this, we have also conducted bacterial culture experiments using unloaded (no-TCH) scaffolds. As shown in Fig. S10, SEM images of P:P, 1:1, and 1:3 scaffolds cultured for 24 hours with *E. coli*, *P. aeruginosa*, and *S. aureus* reveal distinct differences in bacterial colonization. As expected, the P:P scaffold exhibits the lowest antibacterial activity, with extensive bacterial growth covering the scaffold surface across all strains. In contrast, scaffolds containing MXene demonstrate a marked reduction in bacterial presence, though the extent varied depending on the bacterial strain, likely due to differences in adhesion mechanisms and strain-specific susceptibility. These findings confirm that MXene itself imparts direct antibacterial effects and plays an active role in enhancing the surface antimicrobial properties of the composite scaffolds.

### 3.5. EIS monitoring of bacterial growth

EIS is a versatile technique that can monitor changes at the cell–electrode interface, providing information on proliferation, adhesion, and functional responses. Its non-destructive and real-time nature makes it particularly valuable for dynamic monitoring of biological processes.[15,43,46,47] Building on this, we adapt EIS characterization to evaluate bacterial interactions, specifically with *E. coli* within the studied scaffolds, whilst using their inherent electrically conducting nature. A custom-made three-electrode electrochemical setup is employed, as shown in Fig. 5a, enabling *in situ*, real-time monitoring of bacterial proliferation by correlating changes in the impedance magnitude. The scaffold acts as the working electrode (WE) through lateral gold contact, while a stainless-steel mesh and an Ag/AgCl electrode were used as the counter (CE) and reference (RE) electrodes, respectively. For comparison, EIS measurements have been conducted in three systems, P:P, P:P/MXene 1:1, and 1:3, with data collected at different time points. Fig. 5b shows the evolution of the EIS Bode plots over a 16 h period, highlighting changes in impedance behavior. Both the P:P and 1:1 scaffolds exhibit a noticeable increase in the overall impedance magnitude across the frequency spectrum, with the most prominent changes occurring in the low- to mid-frequency regimes, associated with interfacial processes such as bacterial adhesion and proliferation. In contrast, the 1:3 scaffold displays a remarkably stable impedance profile at both early and extended timepoints, indicating minimal bacterial attachment. This electrochemical response is consistent with the previous observations, confirming the role of MXene in suppressing bacterial attachment and growth. These properties are assessed by tracking changes in the characteristic resistance, denoted as $R_b$, which reflects the overall resistance of the electrode (scaffold and bacteria/biofilm formation). This is extracted by fitting the Nyquist plots using a simplified Randle circuit model (see Fig. 5c), consisting of the solution resistance ($R_s$), the scaffold-biofilm mixed resistance ($R_b$), and a constant phase element (CPE) to account for a non-ideal capacitor. The comparative Nyquist plots at 0 h and 16 h, along with the corresponding fitted data, display a characteristic semicircular arc whose diameter directly correlates with the $R_b$ resistance at the electrode–electrolyte interface. An increase in this semicircle diameter over time corresponds to greater resistance, associated with bacterial proliferation. Specifically, the P:P scaffold shows an increase in $R_b$ from 61.6 Ω to 176.4 Ω, while the 1:1 scaffold exhibits a rise from 305.9 Ω to 501.7 Ω. These changes indicate significant bacterial attachment and growth on the scaffold surfaces over the 16-hour period. In contrast, the 1:3 scaffold exhibits minimal changes, with the values decreasing from 14.9 kΩ to 14.2 kΩ and an incomplete semicircle, suggesting a relatively stable electrochemical behavior and no significant bacterial growth. This response aligns well with the $OD_{600}$ measurements and the SEM imaging.

Furthermore, the evolution of the cumulative percentage change in $R_b$ for both non-TCH and TCH-loaded scaffolds is shown in Fig. 5d, indicating the effectiveness of TCH-loaded scaffolds in suppressing bacterial growth. Specifically, a pronounced difference is observed at the 16-hour time point, where TCH-loaded scaffolds show a significantly lower increase in $R_b$ compared to their non-loaded counterparts, indicating effective suppression of bacterial growth. Furthermore, within the TCH-loaded group, MXene-based scaffolds exhibit a notably smaller change in $R_b$ compared to the pristine P:P scaffolds, suggesting enhanced antibacterial performance.

It is worth mentioning that each bacterial strain is expected to have a distinct EIS profile, determined by factors such as adhesion, growth dynamics, and secretion behaviour. For example, the production of extracellular polymeric substances can affect how a strain interacts with the scaffold surface and the surrounding electrolyte. Strains that rapidly adhere and form dense biofilms may have a tendency to increase interfacial resistance and capacitive behaviour more prominently due to the insulating nature of the biofilm layer. In contrast, less adherent or slower-growing bacteria, such as *E. coli* under certain conditions, may exhibit a delayed or weaker EIS response. In this regard, our platform offers a unique opportunity to identify various bacteria-associated EIS signature profiles.

### 3.6. Drug release control through electrical stimulation

To assess the electro-responsiveness of the scaffolds and their capability to electrically trigger drug release, P:P/MXene scaffolds have been subjected to pulsed-DC electrical stimulation in PBS over 16 hours (see Fig. 6a). The CPD profiles under

Open Access Article. Published on 26 September 2025. Downloaded on 6/16/2026 10:00:02 AM.
This article is licensed under a Creative Commons Attribution-NonCommercial 3.0 Unported Licence.

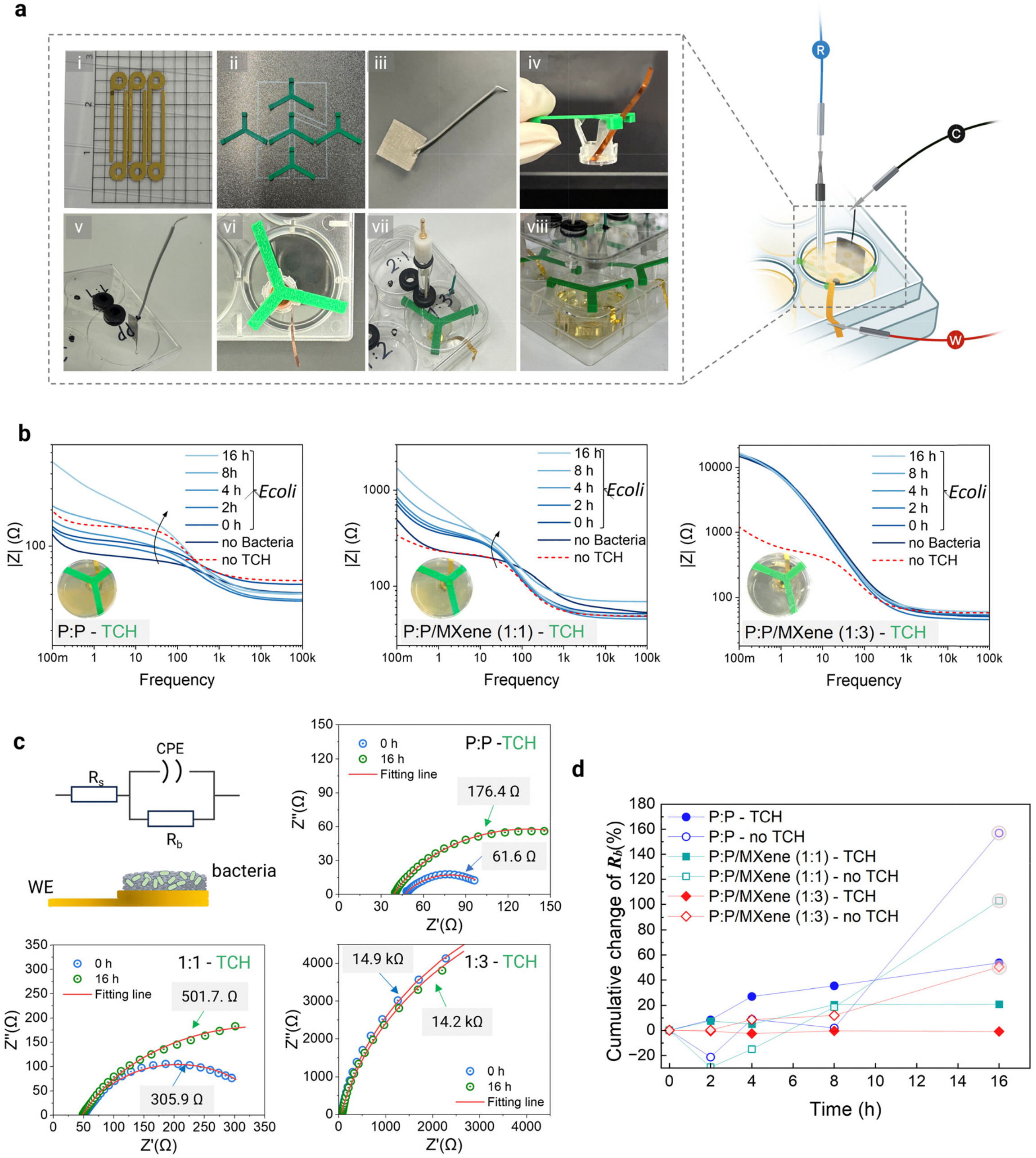

Fig. 5 (a) Device components for measuring scaffold-based electrodes. (i) Au base electrode, (ii) insert holder, (iii) counter mesh electrode, (iv) well plate insert with gold electrode and scaffold, (v) counter mesh electrode integrated in the lid, (vi) insert integration in the well, (vii) complete assembly, (viii) photo of the bioelectronic setup during bacterial measurements. The schematic shows the 3-electrode EIS configuration used in this work. (b) Bode plot spectra curves at different time points and conditions for pristine (P : P), 1 : 1, and 1 : 3 TCH-loaded scaffolds. Insets show the corresponding photos of the wells after 16 h of scaffold in the bacterial (*E. coli*) medium. (c) Nyquist plots and corresponding curve fitting for the EIS measurements of the scaffolds, at 0 h and at 16 h. The schematic shows the equivalent circuit model used for the fitting and estimation of the impedance parameters ($R_b$, CPE), as well as the geometry of the scaffold WE. (d) Graph showing the cumulative % change in the fit-estimated resistance ($R_b$) over time for both the non-TCH (empty symbol) and TCH-loaded scaffolds (filled symbol).

positive, negative, and no-stimulation conditions are shown in Fig. 6b–d for three scaffold compositions: P : P, 1 : 1, and 1 : 3, respectively.

Scaffolds stimulated with a negative voltage (−0.8 V) are found to consistently exhibit the highest CPD of TCH. A possible explanation is that under negative bias, the polymer enters a reduced state wherein electrons are injected into the P : P backbone. To maintain charge neutrality, cations from the electrolyte are introduced into the polymer, compensating for the increased negative charge. This cation uptake further promotes swelling of the scaffold and induces conformational changes within the polymer matrix, which cause pore

Open Access Article. Published on 26 September 2025. Downloaded on 6/16/2026 10:00:02 AM. This article is licensed under a Creative Commons Attribution-NonCommercial 3.0 Unported Licence.

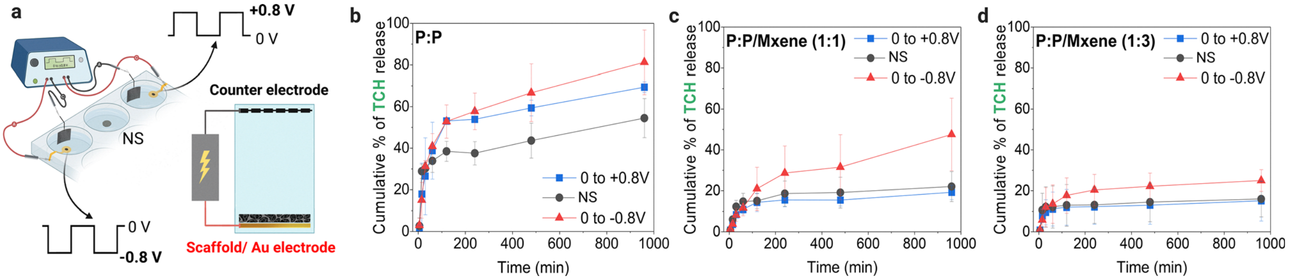

Fig. 6 (a) Schematic illustration of the electrical stimulation setup. Scaffolds are placed in a well plate platform. Two of the wells are connected to a pulse generator to apply +0.8 V or −0.8 V square wave pulses. A Au electrode in contact with the scaffold functions as the working electrode, acting as the anode (at +0.8 V) or the cathode (at −0.8 V), while a metal mesh positioned opposite serves as the counter electrode. The third well serves as a neutral control with no stimulation (NS) applied. (b) Cumulative % TCH release profiles of P : P, and P : P/Mxene scaffolds with ratios of (c) 1 : 1, and (d) 1 : 3 over time under negative (−0.8 V), positive (+0.8 V), and NS conditions.

expansion or disruption of non-covalent interactions, thereby enhancing TCH release. This is consistent with previous reports demonstrating the effects of redox alterations on morpho-structural properties of P : P.[48] Notably, this effect is substantially lower in the MXene-based scaffolds, with the 1 : 3 scaffold showing the smallest response. This is most likely due to alterations in the redox activity of the composite scaffolds and shielding effects caused by the presence of rigid MXene domains, restricting the pore opening and the subsequent TCH release. Notably, in the case of positive pulsed stimulation (+0.8 V), in the oxidation state, a relative increase *versus* the no-stimulation condition is observed only in the case of P : P, while it is found to suppress or not affect the release in the MXene-based scaffolds.

While further studies are required to fully investigate the effect of electrostimulation on drug release, our findings highlight the potential of P : P/MXene scaffolds as a controlled and on-demand drug delivery system.

## 4. Conclusions

This study presents the development of multifunctional P : P/MXene composite scaffolds designed for infection-responsive drug delivery applications. By combining the electrical conductivity of P : P with the structural and intrinsic antibacterial properties of MXene, we engineered a 3D bioactive platform capable of antibiotic release, bacterial inhibition, real-time electrochemical monitoring, and electrically triggered drug release. This combination effectively restricts bacterial adhesion and early proliferation, while the sustained release of TCH further inhibits biofilm formation.

Antibacterial assays confirmed superior efficacy against both Gram-negative and Gram-positive bacteria, attributed to the synergistic effects of TCH release and MXene's inherent antimicrobial activity. Moreover, *in situ* impedance-based sensing was found to provide a non-invasive and real-time approach for monitoring bacterial growth. Finally, we explored the use of electrical stimulation to trigger on-demand drug release, providing an extra layer of control over therapeutic delivery. Future studies will focus on *in vivo* validation, long-term biocompatibility, and optimization of electrical stimulation protocols to support clinical translation.

## Author contributions

Conceptualization: C. P., K. H. A. Funding acquisition: C. P. Project administration: C. P. Resources: C. P., A. A. S. Supervision: C. P. Data curation: K. H. A, S. B. A, CP. Formal analysis: K. H. A, S. B. A, C. P., Investigation: K. H. A, D. I, S. B. A, Methodology: K. H. A, S. B. A, B. F., D. I, C. P. Validation: K. H. A, D. I, C. P. Software: K. H. A, C. P Visualization: K. H. A, C. P. Writing – original draft: K. H. A, C. P.

All co-authors contributed to the original draft. Writing – review and editing: All coauthors contributed to reviewing and editing

## Conflicts of interest

There are no conflicts to declare.

## Data availability

All data supporting this study are available in the manuscript and Supplementary Information, which includes scaffold fabrication details, SEM images, pore size analysis, heightmaps, conductivity, and swelling behavior. See DOI: **https://doi.org/10.1039/d5tb00955c**

## Acknowledgements

This project is co-funded by Khalifa University, Abu Dhabi, United Arab Emirates (UAE), Al Jalila Foundation, and Sandooq Al Watan (SWARD) under grant codes 5032-FSU-2022-007, AJF-2023-175, and SWARD-F23-021/PRJ-SWARD-691, respectively. This work is partially supported by STRATA Manufacturing PJSC and supported by the Advanced Research and Innovation Center (ARIC), which is jointly funded by Aerospace Holding Company LLC, a wholly-owned subsidiary of Mubadala Investment Company PJSC and Khalifa University of Science & Technology.

Open Access Article. Published on 26 September 2025. Downloaded on 6/16/2026 10:00:02 AM.
This article is licensed under a Creative Commons Attribution-NonCommercial 3.0 Unported Licence.

## References

1 H. M. Bedair, M. Hamed and F. R. Mansour, *Appl. Microbiol. Biotechnol.*, 2024, **108**, 515.

2 M. Haktaniyan and M. Bradley, *Chem. Soc. Rev.*, 2022, **51**, 8584–8611.

3 D. Pranantyo, C. K. Yeo, Y. Wu, C. Fan, X. Xu, Y. S. Yip, M. I. G. Vos, S. H. Mahadevegowda, P. L. K. Lim, L. Yang, P. T. Hammond, D. I. Leavesley, N. S. Tan and M. B. Chan-Park, *Nat. Commun.*, 2024, **15**, 954.

4 A. Ali, M. Govindharaj, B. Fatma, K. H. Alshehhi, D. Islayem, N. B. Alsaafeen, A. M. Pappa and C. Pitsalidis, *Adv. Compos. Hybrid Mater.*, 2025, **8**, 270.

5 Y. Zhang, J. Cui, K.-Y. Chen, S. H. Kuo, J. Sharma, R. Bhatta, Z. Liu, A. Ellis-Mohr, F. An, J. Li, Q. Chen, K. D. Foss, H. Wang, Y. Li, A. M. McCoy, G. W. Lau and Q. Cao, *Sci. Adv.*, 2023, **9**, eadg7397.

6 M. Sánchez-Jiménez, F. Estrany, N. Borràs, B. Maiti, D. D. Díaz, L. J. del Valle and C. Alemán, *Soft Matter*, 2019, **15**, 7695–7703.

7 S. Gupta, R. Datt, A. Mishra, W. C. Tsoi, A. Patra and P. Bober, *J. Appl. Polym. Sci.*, 2022, **139**, e52663.

8 K. Rasool, M. Helal, A. Ali, C. E. Ren, Y. Gogotsi and K. A. Mahmoud, *ACS Nano*, 2016, **10**, 3674–3684.

9 B. Li, Y. Luo, Y. Zheng, X. Liu, L. Tan and S. Wu, *Prog. Mater. Sci.*, 2022, **130**, 100976.

10 X. Lai, Y. Tang, Y. Dong, Y. Luo, X. Yang and Q. Peng, *Adv. NanoBiomed. Res.*, 2024, **4**, 2400033.

11 C. Pitsalidis, A.-M. Pappa, A. J. Boys, Y. Fu, C.-M. Moysidou, D. van Niekerk, J. Saez, A. Savva, D. Iandolo and R. M. Owens, *Chem. Rev.*, 2022, **122**, 4700–4790.

12 A. Koklu, D. Ohayon, S. Wustoni, V. Druet, A. Saleh and S. Inal, *Chem. Rev.*, 2022, **122**, 4581–4635.

13 C. Cea, G. D. Spyropoulos, P. Jastrzebska-Perfect, J. J. Ferrero, J. N. Gelinas and D. Khodagholy, *Nat. Mater.*, 2020, **19**, 679–686.

14 A. J. Boys, A. Carnicer-Lombarte, A. Güemes-Gonzalez, D. C. van Niekerk, S. Hilton, D. G. Barone, C. M. Proctor, R. M. Owens and G. G. Malliaras, *Adv. Mater.*, 2023, **35**, 2207847.

15 C. Pitsalidis, D. van Niekerk, C.-M. Moysidou, A. J. Boys, A. Withers, R. Vallet and R. M. Owens, *Sci. Adv.*, 2022, **8**, eabo4761.

16 R. A. Nasser, S. S. Arya, K. H. Alshehhi, J. C. M. Teo and C. Pitsalidis, *Trends Biotechnol.*, 2024, **42**, 760–779.

17 S. Inal, A. Hama, M. Ferro, C. Pitsalidis, J. Oziat, D. Iandolo, A.-M. Pappa, M. Hadida, M. Huerta, D. Marchat, P. Mailley and R. M. Owens, *Adv. Biosyst.*, 2017, **1**, 1700052.

18 A. Savva, J. Saez, A. Withers, C. Barberio, V. Stoeger, S. Elias-Kirma, Z. Lu, C.-M. Moysidou, K. Kallitsis, C. Pitsalidis and R. M. Owens, *Mater. Horiz.*, 2023, **10**, 3589–3600.

19 C. Pitsalidis, M. P. Ferro, D. Iandolo, L. Tzounis, S. Inal and R. M. Owens, *Sci. Adv.*, 2018, **4**, eaat4253.

20 C.-M. Moysidou, C. Pitsalidis, M. Al-Sharabi, A. M. Withers, J. A. Zeitler and R. M. Owens, *Adv. Biol.*, 2021, **5**, 2000306.

21 A. K. Jayaram, C. Pitsalidis, E. Tan, C.-M. Moysidou, M. F. L. D. Volder, J.-S. Kim and R. M. Owens, *Front. Chem.*, 2019, **7**, 363.

22 P. Xue, C. Valenzuela, S. Ma, X. Zhang, J. Ma, Y. Chen, X. Xu and L. Wang, *Adv. Funct. Mater.*, 2023, **33**, 2214867.

23 Y.-C. Chen, Y.-F. Lin, C.-T. Liu, Y.-C. Liu, M.-H. Lin, G.-Y. Lan, Y.-S. Cheng, H.-L. Yu, C.-C. Huang, H.-T. Chang, N.-C. Cheng, Y.-S. Hsiao and J. Yu, *ACS Appl. Polym. Mater.*, 2023, **5**, 4753–4766.

24 A. Pappa, V. F. Curto, M. Braendlein, X. Strakosas, M. J. Donahue, M. Fiocchi, G. G. Malliaras and R. M. Owens, *Adv. Healthcare Mater.*, 2016, **5**, 2295–2302.

25 E. Bihar, S. Wustoni, A. M. Pappa, K. N. Salama, D. Baran and S. Inal, *npj Flex. Electron.*, 2018, **2**, 30.

26 M. E. Alkahtani, M. Elbadawi, C. A. R. Chapman, R. A. Green, S. Gaisford, M. Orlu and A. W. Basit, *Adv. Healthcare Mater.*, 2024, **13**, 2301759.

27 N. Lopez-Larrea, S. Wustoni, M. I. Peñas, J. Uribe, A. Dominguez-Alfaro, A. Gallastegui, S. Inal and D. Mecerreyes, *Adv. Funct. Mater.*, 2024, **34**, 2403708.

28 Y. Fang, N. Qiao, H. Deng, M. Ren, Y. Zhang, D. Zhang, H. Lin, Y. Chen, K. T. Yong and J. Xiong, *Adv. Mater. Technol.*, 2022, **7**, 2200103.

29 Y.-S. Hsiao, E. D. Quiñones, S.-C. Yen, J. Yu, J.-T. Fang, P. Chen and R.-S. Juang, *ACS Appl. Mater. Interfaces*, 2023, **15**, 21953–21964.

30 B. Anasori and Y. Gogotsi, *Graphene 2D Mater.*, 2022, **7**, 75–79.

31 A. VahidMohammadi, J. Rosen and Y. Gogotsi, *Science*, 2021, **372**, eabf1581.

32 I.-C. Lee, Y.-C. E. Li, J. L. Thomas, M.-H. Lee and H.-Y. Lin, *Mater. Horiz.*, 2023, **11**, 876–902.

33 L. Fusco, A. Gazzi, C. E. Shuck, M. Orecchioni, E. I. Ahmed, L. Giro, B. Zavan, A. Yilmazer, K. Ley, D. Bedognetti, Y. Gogotsi and L. G. Delogu, *Small Methods*, 2023, **7**, e2300197.

34 Y. Liu, Q. Han, W. Yang, X. Gan, Y. Yang, K. Xie, L. Xie and Y. Deng, *Mater. Sci. Eng., C*, 2020, **116**, 111212.

35 H. Rastin, B. Zhang, A. Mazinani, K. Hassan, J. Bi, T. T. Tung and D. Losic, *Nanoscale*, 2020, **12**, 16069–16080.

36 K. Diedkova, A. D. Pogrebnjak, S. Kyrylenko, K. Smyrnova, V. V. Buranich, P. Horodek, P. Zukowski, T. N. Koltunowicz, P. Galaszkiewicz, K. Makashina, V. Bondariev, M. Sahul, M. Caplovicova, Y. Husak, W. Simka, V. Korniienko, A. Stolarczyk, A. Blacha-Grzechnik, V. Balitskyi, V. Zahorodna, I. Baginskiy, U. Riekstina, O. Gogotsi, Y. Gogotsi and M. Pogorielov, *ACS Appl. Mater. Interfaces*, 2023, **15**, 14033–14047.

37 N. B. Alsaafeen, S. S. Bawazir, K. K. Jena, A. Seitak, B. Fatma, C. Pitsalidis, A. Khandoker and A.-M. Pappa, *ACS Appl. Mater. Interfaces*, 2024, **16**, 61435–61445.

38 U. Amara, I. Hussain, M. Ahmad, K. Mahmood and K. Zhang, *Small*, 2023, **19**, e2205249.

39 C. Wang and J.-J. Jian, *J. Water Environ. Technol.*, 2015, **13**, 325.

This journal is © The Royal Society of Chemistry 2025

Open Access Article. Published on 26 September 2025. Downloaded on 6/16/2026 10:00:02 AM. This article is licensed under a Creative Commons Attribution-NonCommercial 3.0 Unported Licence.

40 S. Inal, A. Hama, M. Ferro, C. Pitsalidis, J. Oziat, D. Iandolo, A. Pappa, M. Hadida, M. Huerta, D. Marchat, P. Mailley and R. M. Owens, *Adv. Biosyst.*, 2017, **1**, 1700052.

41 C. Moysidou, C. Pitsalidis, M. Al-Sharabi, A. M. Withers, J. A. Zeitler and R. M. Owens, *Adv. Biol.*, 2021, **5**, 2000306.

42 D. Iandolo, J. Sheard, G. K. Levy, C. Pitsalidis, E. Tan, A. Dennis, J.-S. Kim, A. E. Markaki, D. Widera and R. M. Owens, *MRS Commun.*, 2020, **10**, 179–187.

43 C.-M. Moysidou, D. C. van Niekerk, V. Stoeger, C. Pitsalidis, L. A. Draper, A. M. Withers, K. Hughes, R. McCoy, R. Acharya, C. Hill and R. M. Owens, *Small Sci.*, 2024, **4**, 2300349.

44 J. N. Walker and A. R. Horswill, *Front. Cell. Infect. Microbiol.*, 2012, **2**, 39.

45 J. L. Lister and A. R. Horswill, *Front. Cell. Infect. Microbiol.*, 2014, **4**, 178.

46 V. F. Curto, B. Marchiori, A. Hama, A.-M. Pappa, M. P. Ferro, M. Braendlein, J. Rivnay, M. Fiocchi, G. G. Malliaras, M. Ramuz and R. M. Owens, *Microsyst. Nanoeng.*, 2017, **3**, 17028.

47 M. W. van der Helm, O. Y. F. Henry, A. Bein, T. Hamkins-Indik, M. J. Cronce, W. D. Leineweber, M. Odijk, A. D. van der Meer, J. C. T. Eijkel, D. E. Ingber, A. van den Berg and L. I. Segerink, *Lab a Chip*, 2019, **19**, 452–463.

48 F. Amorini, I. Zironi, M. Marzocchi, I. Gualandi, M. Calienni, T. Cramer, B. Fraboni and G. Castellani, *ACS Appl. Mater. Interfaces*, 2017, **9**, 6679–6689.